Electronic Supplementary Material (ESI) for Nanoscale.

Multiscale Modeling of Plasmonic Enhanced Energy Transfer and Cavitation around Laser-Excited Nanoparticles

Adrien Dagallier,[†] Etienne Boulais,[†,‡] Christos Boutopoulos,[†] Rémi Lachaine,[†] and Michel Meunier[*,†]

[†]*Laser Processing and Plasmonics Laboratory, Department of Engineering Physics, Montreal, Quebec, H3C 3A7, Canada*

[‡]*Laboratory of Biosensors and Nanomachines, Department of Chemistry, Montreal, Quebec, H3T 1J4, Canada*

[¶]*SUPA, School of Physics and Astronomy, North Haugh, St. Andrews, KY16 9SS, UK*

E-mail: michel.meunier@polymtl.ca

Phone: +1 (514) 340-4711, ext 4971. Fax: +1 (514) 340-3216

I 3D model details

The model used to compute the 3D energy deposition is based on the one published by Boulais et al.[1] Although it can be applied to any metal, we consider in the following that the nanostructure is made of gold. The electromagnetic field $\mathbf{E}$ is calculated using the Helmholtz equation (1), considering a $\exp(+i\omega t)$ time-harmonic dependency. The electromagnetic wave excites oscillations of the quasi-free electrons in the gold nanostructure, causing both absorption in the particle (Q_{EM}) and redistribution of the incident field in a nanoscale region close to the particle[2]. Owing to the very different heat capacities of the quasi-free electrons and the gold ions, the particle is seen as being composed of a system of electrons and a lattice, following a Two-Temperature Model (TTM)[3], with temperatures T_e and T_{NP} (equations (2,3)). The electronic conductivity C_e is assumed to vary linearly with T_e and the electron-phonon coupling factor G is taken constant[4–6], even if it has been shown that for very large intensities, the behavior of these two parameters changes greatly, due to the excitation of d-band electrons into the conduction band[7].

The extreme laser intensity close to the particle induces the ionization of a small volume of water and formation of a nanoscale plasma[8], whose electronic density and energy density are modeled via equations (4,5)). Water is assumed to behave as an amorphous semiconductor with a 6.5 eV gap[9,10], with a valence and a conduction band. Photoionization through tunnel and multiphoton ionization[11] (S_{photo}) excites electrons from the former to the latter. Excited electrons absorb energy through inverse Brehmsstrahlung[10] (Q_{EM}) and can collide with neighboring water molecules, promoting electrons in the valence band to the conduction band through an avalanche ionization process[12] (S_{coll}). Collisions with ions[13,14] (Q_{ei}) as well as radiative losses[13] (Q_{rad}) and recombination[10] (S_{rec}) complete the possible loss mechanisms. The transient plasma density significantly alters the dielectric permittivity ϵ_r, strongly coupling the plasma equations (4,5) with Helmholtz equation (1).

Although the TTM is widely used in simulating the irradiation of metals by ultrashort pulses, it does not as such account for the modification of the NP's optical properties during the laser pulse[15–19]. As of today, fudge factors for *ad hoc* fitting are often used[15,20] when modeling these transient properties and authors use assumptions based on weak intensities (considering only intraband absorption) with temperature changes of a few tens of Kelvins at most[17,20–23] that prevent from adapting their model to any irradiation conditions (pulse and particle parameters), in particular those of high intensities than can trigger non-linear absorption in the near-field. Other groups delve into the band structure details and make extensive use of the full Boltzmann equations[18,24–26], but computational costs rise accordingly.

A reliable model that includes both the transient metal optical properties and the modification of the medium permittivity due to the excitation of quasi-free electrons close to the surface in the context of plasmon-enhanced cavitation is not currently available. From the results from our training set, we observed that there is between 10 and 20 times more energy deposited around the particle as compared to in the particle, and the particle temperature stays well below the melting threshold, in agreement with experimental measurement of the particle breaking threshold[27]. Furthermore, the modifications of the NP properties are mostly concentrated in the wavelength window from 450 nm to 650 nm for AuNPs[15–19] (it is the d–s or p interband transition), so irradiation at wavelengths outside of this window are much less affected. We therefore chose to keep the TTM approach. Our model will thus tend to slightly overestimate the energy deposited directly in the particle for high intensities, which should result in bubbles slightly bigger than observed experimentally in the case of conduction-mediated bubbles.

Both the plasma and the particle transfer heat to the water, inducing a temperature rise that is modeled using a classical heat equation (equation (6)). The thermodynamic transition is assumed to be isochoric, due to the pulse widths being shorter than the water molecules collision time[10]. These equations are solved with the finite-element method software Comsol (Comsol, Inc., Burlington) in a domain of radius corresponding to the irradiation wavelength. Perfectly Matched Layers are used to emulate an infinite domain. Complete geometry tallies up to $\simeq$45,000 tetrahedral second order elements. A Generalized-α solver with Comsol's default settings is used for time-stepping. The equations are presented in Table S1, the numerous terms in these equations are detailed in Table S2.

Table S1 | Equations for the 3D modeling of the energy deposition following the laser pulse

$\mathbf{E}$	Complex electromagnetic field	$\nabla \times (\nabla \times \mathbf{E}) - k_0^2 \epsilon_r \mathbf{E} = 0$	(1)
T_e	Temperature of the particle quasi-free electrons	$C_{v,e} \dot{T}_e - \nabla \cdot (k_e \nabla T_e) = Q_{EM} - \Gamma(T_e - T_{NP})$	(2)
T_{NP}	Temperature of the particle	$\begin{cases} C_{NP} \rho_{NP} \dot{T}_{NP} - \nabla \cdot (k_{NP} \nabla T_{NP}) & = -\Gamma(T_e - T_{NP}) \\ \mathbf{n} \cdot (C_{NP} \nabla T_{NP}) & = g(T_w - T_{NP}) \end{cases}$	(3)
n_e	Plasma electronic density	$\dot{n}_e + \nabla \cdot j^n = S_{photo} + S_{coll} + S_{rec}$	(4)
u	Plasma energy density	$\dot{u} + \nabla \cdot j^q = Q_{EM} - Q_{ei} - Q_{rad} - \tilde{\Delta} \times S_{coll}$	(5)
T_w	Water temperature, isochoric heating	$\begin{cases} C_w \rho_\infty \dot{T}_w - \nabla \cdot (k_w \nabla T_w) & = Q_{ei} + (\tilde{\Delta} + \frac{u}{n_e}) \times S_{rec} \\ \mathbf{n} \cdot (C_w \nabla T_w) & = -g(T_w - T_{NP}) \end{cases}$	(6)

Table S2 | Parameters used for the 3D simulation of the interaction of a gold nanoparticle and an ultrafast laser

$\mathbf{n}$	Normal unit vector	
ϵ_r	Complex permittivity, SiO_2	2.1
ϵ_r	Complex permittivity, gold	from Johnson & Christy[28]
ϵ_r	Complex permittivity, water	$\left[n_w^2 - \frac{\omega_p^2}{\omega^2 + \nu_e^2}\right] - i \left[\frac{\omega_p^2 \nu_e}{\omega^3 + \omega \nu_e^2}\right]$
n_w	Water refractive index at 800(400) nm	1.328(1.343)
E_{laser}	Incident laser electromagnetic field	$E_t \exp(-i n_w k_0 x) \vec{z}$
E_t	Field amplitude	$\sqrt{\frac{2I_0}{n_w c \epsilon_0} \exp(-4\ln(2)(\frac{t - 1.5\, fwhm}{fwhm})^2)}$

$fwhm$	Laser pulse full width at half maximum	Defined by user
I_0	Intensity of the laser field	$\frac{F}{fwhm}\sqrt{\frac{4\ln(2)}{\pi}}$
F	Laser fluence	Defined by user
λ	Irradiation wavelength	Defined by user
ω	Angular frequency	$\frac{2\pi c}{\lambda}$
c	Velocity of light in vacuum	299,792.458 m/s
m_e	Mass of the electron	$9.1094\,10^{-31}$ kg
k_B	Boltzmann constant	$1.3806\,10^{-23}$ J/kg
$\hbar$	Planck constant	$1.0546\,10^{-34}$ J.s
e	Elementary charge	$1.6022\,10^{-19}$ C
ϵ_0	Vacuum permittivity	$8.8542\,10^{-12}$ F/m
S_{photo}	Photoionization rate, from Keldysh theory[11]: $\frac{2\omega}{9\pi}(n_0 - n_e)\left(\frac{\sqrt{1+\gamma^2}}{\gamma}\frac{m_{eq}\omega}{\hbar}\right)^{3/2} \times Q(\gamma, \frac{\tilde{\Delta}}{\hbar\omega}) \times \exp\left(-\pi\left\langle\frac{\tilde{\Delta}}{\hbar\omega}+1\right\rangle\frac{K\left(\frac{\gamma}{\sqrt{1+\gamma^2}}\right)-E\left(\frac{\gamma}{\sqrt{1+\gamma^2}}\right)}{E\left(\frac{1}{\sqrt{1+\gamma^2}}\right)}\right)$ With $\langle x\rangle$ = integer part of x	

$Q(\gamma, x)$	$\sqrt{\frac{\pi}{2K\left(\frac{1}{\sqrt{1+\gamma^2}}\right)}} \times \sum_{l=0}^{\infty} \phi\left(\sqrt{\frac{\pi^2(2\left\langle x+1\right\rangle - 2x+1)}{2E\left(\frac{1}{\sqrt{1+\gamma^2}}\right)K\left(\frac{1}{\sqrt{1+\gamma^2}}\right)}}\right) \times \exp\left(-\pi l \frac{K\left(\frac{\gamma}{\sqrt{1+\gamma^2}}\right) - E\left(\frac{\gamma}{\sqrt{1+\gamma^2}}\right)}{E\left(\frac{1}{\sqrt{1+\gamma^2}}\right)}\right)$	
$E(x)$	Elliptic integral of the first kind	$E(x) = \int_0^1 \frac{\sqrt{1-\theta^2 x^2}}{\sqrt{1-\theta^2}} \mathrm{d}\theta$
$K(x)$	Elliptic integral of the second kind	$K(x) = \int_0^1 \frac{\mathrm{d}\theta}{\sqrt{1-\theta^2 x^2}\sqrt{1-\theta^2}}$
$\phi(x)$	Dawson probability integral	$\phi(x) = \int_0^x \exp\left(y^2 - x^2\right) \mathrm{d}y$
γ	Keldysh parameter	$\frac{\omega}{e}\sqrt{\frac{m_{eq}\Delta}{\lvert\mathbf{E}\rvert^2}}$
Δ	Ionization potential[10]	6.5 eV
m_{eq}	Exciton (electron-hole) mass	$\frac{1}{m_{eq}} = \frac{1}{m_e} + \frac{1}{m_h} \simeq \frac{2}{m_e}$
$\tilde{\Delta}$	Effective ionization potential[11]	$\frac{2}{\pi}\Delta\frac{\sqrt{1+\gamma^2}}{\gamma}E\left(\frac{1}{\sqrt{1+\gamma^2}}\right)$
S_{rec}	Recombination rate[10]	τn_e^2
τ	Plasma recombination constant[10,29]	$2\,10^{-9}$ cm^{3}s^{-1}
j^n	Electron current density	$D_e \nabla n_e$
D_e	Electron density diffusion coefficient	$\frac{k_B T_p}{m_e(\nu_{ei} + \nu_{en})}$
T_p	Plasma temperature[12]	$\frac{1}{3}\frac{m_e v_e^2}{k_B}$
ν_{ei}	Plasma collision frequency with ions[30]	$\min\left\{\sqrt{\frac{\omega_p^2}{6}}, \frac{n_e e^4 \Lambda}{3\epsilon_0^2\sqrt{m_e(2\pi k_B T_p)^3}}\right\}$
ν_{en}	Plasma collision frequency with neutral species[12,13]	$\min\left\{n_a \sigma_a v_e, \frac{1}{2}v_e(\frac{4\pi}{3}n_a)^{1/3}\right\}$

n_a	Density of neutral species	$\frac{n_0}{2} - \frac{n_e}{2}$
n_0	Valence electron density (water)[10]	$6.68\,10^{22}$ cm^{-3}
σ_a	Collision cross-section with neutral species[31]	$2\,10^{-19}$ m^2
v_e	Mean electron velocity (Maxwell distribution)	$\sqrt{\frac{2u}{m_e n_e}}$
ω_p	Plasma frequency[32]	$\sqrt{\frac{n_e e^2}{m_e \epsilon_0}}$
Λ	Coulomb logarithm[30]	$\max\left\{2, \frac{1}{2}\log\left(1 + \left(\frac{b_{max}}{b_{min}}\right)^2\right)\right\}$
b_{max}	Maximal impact factor[30]	$\left(\frac{n_e e^2}{\epsilon_0 k_B \sqrt{T_p^2 + T_F^2}} + \frac{n_e e^2}{\epsilon_0 k_B T_w}\right)^{-1}$
b_{min}	Minimal impact factor[13,30]	$\max\left\{\frac{e^2}{4\pi\epsilon_0 m_e v_e^2}, \frac{\pi\hbar}{m_e v_e}\right\}$
T_F	Fermi temperature[33]	$\frac{\hbar}{2m_e k_B}(3\pi^2 n_e)^{2/3}$
S_{coll}	Collision ionization rate[12]	$n_e \nu_c$
ν_c	Collision ionization frequency[12]: $\max\left\{0, n_a\sigma_c v_e\left((7.5\beta - 1)\sqrt{\frac{\beta}{\pi}}\exp(-1/\beta) + (3.75\beta^2 - 3\beta + 1)(1 - erf(1/\sqrt{\beta}))\right)\right\}$	
σ_c	Collision ionization cross-section[34]	$8.97\,10^{-22}$ m^2
β	Normalized kinetic energy[12]	$\frac{3}{2}\frac{k_B T_p}{\tilde{\Delta}}$
Q_{ei}	Electron-ion energetic coupling[13,14]	$3k_B \frac{m_e}{m_{molec}} n_e \nu_e (T_p - T_w)$
m_{molec}	Mass of one water molecule	$2.99\,10^{-26}$ kg
Q_{rad}	Radiative losses[14]	$\frac{e^2(k_B T_p)^2}{\pi\epsilon_0\sqrt{3}\hbar m_e c^3} n_e \nu_e$
ν_e	Total collision frequency	$\nu_{ei} + \nu_{en}$
j^q	Energy density flux	$D_u \nabla u$
D_u	Plasma energy diffusion coefficient	$\frac{5}{3} D_e$
Q_{EM}	Electromagnetic losses[32]	$\frac{1}{2} Re\left\{\langle \mathbf{J} \cdot \mathbf{E} \rangle\right\}$

$\mathbf{J}$	Current density[13,31,33]	$\sigma_{cond}\mathbf{E}$
σ_{cond}	Electrical conductivity[13,31,33]	$\frac{n_e e^2}{m_e \nu_e} \frac{1}{1 + i\omega/\nu_e}$
ρ_∞	Constant water density	998.2 kg/m^3
C_w	Water heat capacity at constant volume	$f(T_w)$, from IAPWS[35] and SESAME[36]
k_w	Water heat conductivity	$f(T_w)$, from IAPWS[35]
g	Heat transfer coefficient at the gold-water interface	$101.2\,10^6$ W/m^2/K, from optimization
ρ_{NP}	Particle density (given for gold)	19,300 kg/m^3
C_{NP}	Particle heat capacity (given for gold[4])	$109.579 + 0.128T_{NP} - 3.4\,10^{-4}T_{NP}^2 + 5.24\,10^{-7}T_{NP}^3 - 3.93\,10^{-10}T_{NP}^4 + 1.17\,10^{-13}T_{NP}^5$ W/kg/K for T_{NP}<1337 K, constant above 1337 K
k_{NP}	Particle thermal conductivity (gold)	$330.6431 - 0.02536626T_{NP} - 3.4\,10^{-4}T_{NP}^2 + 5.24\,10^{-7}T_{NP}^3 - 3.93\,10^{-10}T_{NP}^4 + 1.17\,10^{-13}T_{NP}^5$ J/kg/K for T_{NP}<1337 K, constant above 1337 K
Γ	Electron-phonon coupling[24]	$2.5\,10^{16}$ W/m^3/K
k_e	Electron heat conductivity in gold[37]	2000 W/m/K
$C_{v,e}$	Electron heat capacity in gold[4–6,38,39]	$T_e \times 70$ [J/m^3/K^2]

The energy deposition is then extracted from the previous calculations. In the particle, the energy deposition is the integral of the electromagnetic rate of work Q_{EM}: $E_{dep,NP} = \int \iiint_{NP} Q_{EM} \mathrm{d}V \mathrm{d}t$. The energy deposited in the plasma is the sum of the energy absorbed through inverse Brehmsstrahlung Q_{EM} and the energy absorbed from photoionization, yielding $E_{dep,pl} = \int \iiint\limits_{water} (Q_{EM} + \tilde{\Delta} \times S_{photo}) \mathrm{d}V \mathrm{d}t$.

II Cavitation

The second step of our framework concerns the cavitation onset, that is to say the link between the 1 - 10 ps energy deposition in the nanostructure-water system and the 100 ps – 100 ns bubble evolution.

In this sub-model, we calculate the energy deposited in the water-nanostructure system, find the energy that dissipates in the shockwave and is therefore not transferred to the bubble and determine the thermodynamic variables necessary for the bubble dynamics, namely the initial bubble radius, wall velocity, bubble density, bubble energy and particle temperature.

In the particle, the energy deposition is simply the integral of the electromagnetic rate of work $E_{dep,NP} = \int \iiint\limits_{NP} Q_{EM} \mathrm{d}V \mathrm{d}t$. The energy deposited in the plasma is the sum of the energy absorbed through inverse Brehmsstrahlung Q_{EM} and the energy absorbed from photoionization, yielding $E_{dep,pl} = \int \iiint\limits_{water} (Q_{EM} + \tilde{\Delta} \times S_{photo}) \mathrm{d}V \mathrm{d}t$.

These two energy sources operate on different timescales and at different locations around the particle: conduction heats a layer around the structure while plasma heats up the fluid in the near-field region, which changes with the wavelength, light polarization or particle geometry. They are therefore considered separately (Figure S1).

There are two limiting cases: when $E_{dep,NP} << E_{dep,pl}$, and when $E_{dep,NP} >> E_{dep,pl}$. A representative modeling lies between these two regimes, symbolized by the arrows in Figure S1a. This mathematically translates in a weighted average of the thermodynamic and kinetic properties of the two heated volumes. In the following, we will therefore calculate these properties in the two limiting cases and then describe how the real case is recovered from the two limits.

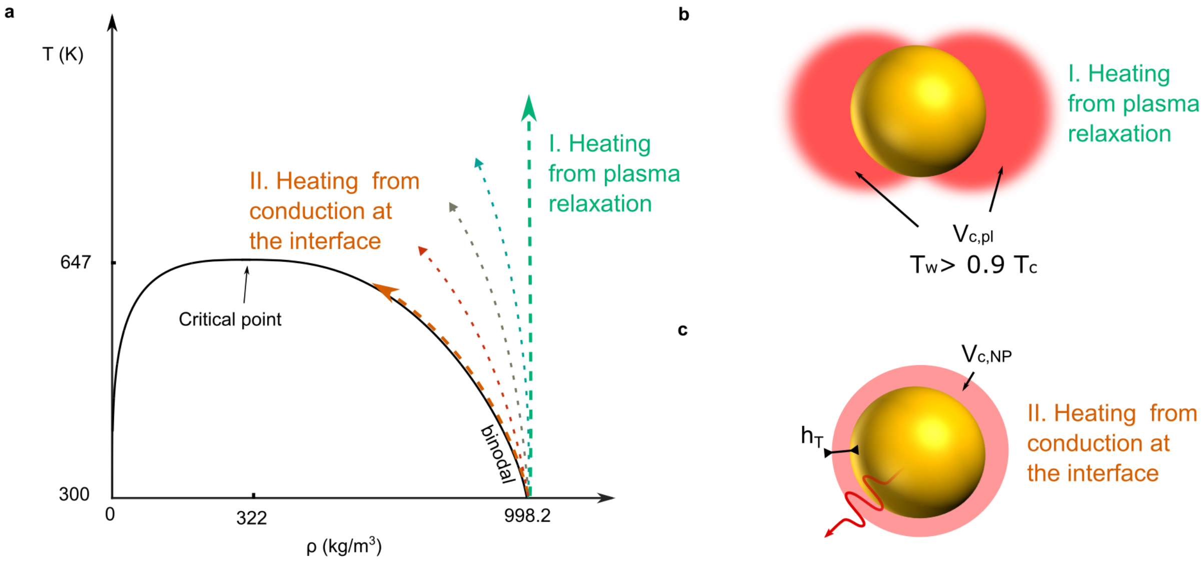

Figure S1 | Determination of the initial thermodynamic variables. **(a)** Trajectories in water phase diagram for various ratios of the energy deposition in the plasma and in the nanoparticle. Plasma heating translates in an isochoric transition (vertical line), whereas conduction-only heat transfer is assumed to follow the binodal. **(b)** Plasma-mediated isochoric heating. **(c)** Conductive heat transfer along the binodal

II.A First case: Heating from plasma relaxation ($E_{dep,NP} << E_{dep,pl}$)

In the first case, an isochoric heating takes place. Water temperature rises extremely fast (≃1-10 ps) and very locally, generating strong stress confinement and large amplitude shockwaves. The characteristic variable that we consider is a critical volume V_c where the temperature is above 0.9 T_c (Figure S1b), with $T_c = 647.096$ K the critical temperature of water. Since the transformation is isochoric, the density ρ_{pl} in that volume is ρ_∞ and its mass $m_{pl} = \rho_{pl} V_{c,pl}$. Knowing T_{pl} and ρ_{pl}, we can deduce the pressure $p_{pl} = f(T_{pl}, \rho_{pl})$ from IAPWS[35] and SESAME[36] equations of state. From there, Rankine-Hugoniot relations yields the velocity of the particles in the wake of the shockwave, which is usually associated to the initial bubble wall velocity[40,41].

If p_{pl} is the shockwave pressure and v_{Spl} its velocity, Rankine-Hugoniot equation reads: $v_{Spl} \times (10^{(v_{Spl}-c_{s0})/c_2} - 1) = \frac{p_{pl}-p_\infty}{\rho_\infty c_1}$, where c_{s0}=1484 m/s is the velocity of the sound at (ρ_∞, p_∞) and c_1=5190 m/s and c_2=25306 m/s are two empirical constants[40,41].

II.B Second case: Heating from conduction at the interface ($E_{dep,NP} >> E_{dep,pl}$)

In the second case, a thin shell of water around the particle is heated along the binodal. This energy transfer being much slower than the energy deposition in the plasma (the electronic and lattice temperature equilibrate after ≃50 ps, the equilibrium with the temperature of the water is reached after ≃500 ps), the initial 3D simulation can only account for the energy absorption by the particle quasi-free-electrons. We therefore need to calculate separately the evolution of the electronic, lattice and water temperatures in and around the particle, respectively. The two former are computed with the very same TTM as in the 3D model (equations (7,8)). The last equation is written for the entropy of the liquid shell S_w around the particle. Since the water volume is on the binodal, S_w uniquely defines a temperature T_w as well as a density ρ_w via the IAPWS equation of state[35]. Note that the thickness of the shell h_T as well as the g factor in equations (8,9) are parameters given by the optimization.

Table S3 | Equations for the conductive heat transfer

T_e	Temperature of the gold quasi-free electrons	$C_e\rho_e\dot{T}_e = -\Gamma(T_e - T_{NP})$ (7)
T_{NP}	Nanoparticle temperature	$C_{NP}\rho_{NP}\dot{T}_{NP} = \Gamma(T_e - T_{NP} + \frac{3}{R_{NP}}g(T_w - T_{NP}))$ (8)
S_w	Water entropy, heating along the binodal	$m_{h_T}T_w\dot{S}_w = -4\pi R_{NP}^2 g\frac{\rho_w}{\rho_\infty}(T_w - T_{NP})$ (9)

In equation (9), $m_{h_T} = \rho_\infty V_{c,NP}$ is the mass of heated water in the shell and $V_{c,NP} = \frac{4\pi}{3}((R_{NP} + h_T)^3 - R_{NP}^3)$ is the volume of the heated layer. The equation system in Table S3 is solved with Matlab's ode45 solver, with relative and absolute tolerances of 10^{-4}.

The initial water and gold temperature are taken as T_∞, water initial density is ρ_∞. The initial electronic temperature $T_{e,ini}$ is computed via $\int_{T_\infty}^{T_{e,ini}} \rho_e C_e \mathrm{d}T_e = E_{dep,NP}$. This means that we assume that the energy deposition is much faster than the characteristic interaction time of the electrons and the lattice.

The $\frac{\rho_w}{\rho_\infty}$ ratio in (9) comes from the kinetic theory of gases[42]. It scales the energy transfer with the density and eventually cuts it out nearly completely, a behavior observed for instance in molecular dynamics[43] or with small angle X-ray scattering[44]. This last comment naturally defines the integration time range: the simulations stops when $t = \min(\tau_g, \tau_{diffusion})$, where $\tau_g = (\rho_{NP} C_{NP})/3gR_{NP}$ and $\tau_{diffusion} = \rho_\infty C_w / k_w h_T^2$. The former is the characteristic time of heat transfer between the particle and the surrounding water, the latter is the time it takes for heat to diffuse on a h_T distance.

If T_e and T_{NP} are still different, resolution of equations (7) and (8) is continued until the equilibrium is reached, assuming no heat transfer with the water. This final particle temperature serves as an initial condition for the bubble dynamics model.

Knowing the density and the temperature in the water shell, we get the velocity of the conduction-mediated bubble v_{NP} by going through the very same steps as in the previous section. The energy transferred to the water can then be recovered by integration of the heat flux between the particle and the water layer: $E_{NP \to water} = \int -4\pi R_{NP}^2 \, g \, \frac{\rho_w}{\rho_\infty}(T_w - T_{NP})\mathrm{d}t$.

II.C Third case: Intermediate case ($E_{dep,NP} \simeq E_{dep,pl}$)

In this case, energy is transferred to water by both the nanoplasma and the nanostructure. The initial values of the variables for the bubble dynamics are therefore computed as a weighted average between the plasma and temperature variables from the two previous sections.

- The total initial volume is simply $V_{ini} = V_{c,pl} + V_{c,NP}$, the volume above 0.9 T_c plus the volume of the shell of thickness h_T. This gives an initial bubble radius of $R_{ini} = (R_{NP}^3 + \frac{3}{4\pi} V_{ini})^{1/3}$

- The initial density is $\rho_{ini} = \dfrac{m_{h_T} + m_{pl}}{V_{ini}}$
- The initial bubble wall velocity is $v_{ini} = \dfrac{m_{h_T} v_{NP} + \rho_{pl} m_{pl} v_{pl}}{\rho_{ini} V_{ini}}$
- The initial bubble energy requires one last step: to account for the energy that leaves in the pressure wave, we use a law that depends on the energy density, q: $X(q) = \dfrac{1}{1 + \exp(4\ln(3)/\Delta q \, \log_{10} \frac{q_0}{q})}$, where q_0 and Δq are determined in the optimization process, $q_0 = 2.95\, 10^9$ J/m^3 is the inflexion point of the curve and $\Delta q = 1.52$ is defined as the logarithmic width ($\log_{10} q_{90} - \log_{10} q_{10}$) the distance between the points for which $X(q_{10}) = 10\%$ and $X(q_{90}) = 90\%$. The resulting curve is shown in Figure 3 of the main text. The functional form of this pressure wave was kept to a really simple one due to the lack of available data[45].

  For the plasma heating, $q_{pl} = E_{dep,pl}/V_c$, and $X_{pl} = X(q_{pl})$. Similarly for the conduction heating, $q = \dfrac{E_{NP \to w}}{(4\pi/3(R_{NP} + h_T)^3 - R_{NP}^3)}$ and X_{NP} as $X(q_{NP})$. Then the initial bubble energy is $E_{B,ini} = (1 - X_{pl})E_{dep,pl} + (1 - X_{NP})E_{NP \to w}$.

III Bubble Dynamics

Once the initial conditions are determined, the bubble dynamics is computed with a system of coupled ordinary differential equations. The radius of the bubble is calculated using the Gilmore equation (10). A heat and mass transfer equation is used to calculate the evolution of the bubble energy, accounting for heat transfer at the bubble-water and NP-water interfaces (Q_{inter},Q_{NP-w}) and mass transfer at the bubble-water interface (Q_{mass}) (equation (13)), viscous losses (Q_{visc}), the work of pressure (W_p) and surface tension ($Q_{tension}$) (equation (11)). Two thin layers on each side of the bubble wall are used to model the heat transfer. The temperature gradient is assumed to be linear in these regions[46], resulting in a bubble temperature T_B, a temperature at the interface T_{wall} (equation (12)) and the temperature far away from the bubble T_∞. Only conductive heat transfer was taken into account at both NP-vapor and vapor-liquid interfaces. Although significant in some cases, ballistic heat transfer has been shown to be negligible for the bubbles sizes and irradiation conditions used in this work, and was therefore not considered[47].

The contribution of ballistic thermal fluxes becomes significant in two cases:

1) when the bubble is of about the size of the molecules mean free path, about 80 nm under standard atmospheric pressure. At these small sizes, the energy is not transferred through the usual collisions between neighboring molecules, but through collisions at the bubble wall and the particle interface only. Most of our bubbles are much larger (0.8 – 1 μm), and so Fourier's law applies. Moreover, for most of the cases presented in this article, the energy deposition is plasma-mediated and therefore extremely fast and localized. Water undergoes a (kinetic) spinodal decomposition. The initial water density is thus very close to the bulk water one, so the initial mean free path is much shorter than the particle-bubble wall distance and ballistic transfer consequently hardly applies.

2) for small bubbles (R $<$ 100 nm) when the bubble rebounds multiple times. When irradiated by a laser, a hot vapor layer quickly forms around the nanoparticle, *heated by conduction*, effectively slowing down the conductive particle-water energy transfer. The heated vapor layer undergoes a phase change associated to (kinetic) spinodal decomposition and the following growth is commonly described as adiabatic. The bubble then grows and collapses, possibly several times, but the subsequent cycles are not adiabatic anymore and evaporation takes place at the bubble wall. In the case of plasma-mediated bubbles, the initial bubble is much larger, but the phase change is still explosive and the following growth is still adiabatic, so the argument still holds.

Heat transfer at the gold-vapor interface is taken into account (equation (14)). Unless explicitly mentioned otherwise, all the terms regarding the heat and mass transfer at the interface are taken from the work of Kreider et al.[46].

Table S4 | Equations for the bubble dynamics

R	Radius of the bubble	$(1-\frac{\dot{R}}{C})R\ddot{R}+(1-\frac{\dot{R}}{3C})\dot{R}^2=(1+\frac{\dot{R}}{C})H+(1-\frac{\dot{R}}{C})\frac{R}{C}\dot{H}$ (10)
E_B	Bubble energy	$\dot{E}_B=W_p+Q_{inter}+Q_{mass}+Q_{visc}+Q_{tension}+Q_{NP-w}$ (11)
T_{wall}	Liquid water temperature at the bubble wall	$4\pi R^2\left[k_B\frac{T_{wall}-T_B}{\alpha_{\delta i}\times\delta_i}-k_{wall}\frac{T_\infty-T_{wall}}{\alpha_{\delta e}\times\delta_e}\right]+Q_{mass}=0$ (12)
n	Number of water molecules in the bubble	$\dot{n}=\phi_{flux}$ (13)
T_{NP}	Particle temperature	$C_{NP}\rho_{NP}\dot{T}_{NP}=\frac{3g}{R}\frac{\rho_B}{\rho_0}(T_B-T_{NP})$ (14)

Table S5 | Parameters for the bubble dynamics simulation

H	Enthalpy of liquid water	$f(p_{wall},T_{wall})$, from IAPWS[35]
C	Speed of sound at the bubble wall	$f(p_{wall},T_{wall})$, from IAPWS[35]
ρ_{wall}	Water density at the bubble wall	$f(p_{wall},T_{wall})$, from IAPWS[35]
p_{wall}	Pressure of liquid water at the bubble wall	$p_B-\alpha_{visc}\mu\frac{\dot{R}}{R}-\alpha_{tension}\frac{\sigma}{R}$
ρ_B	Density of water inside the bubble	$\frac{nM}{\frac{4\pi}{3}(R^3-R_{NP}^3)}$
R_{NP}	Radius of the nanoparticle	defined by user
ρ_∞	Water density far away from the bubble	998.2 kg/m^3
p_∞	Pressure far away from the bubble	1 bar
T_∞	Temperature far away from the bubble	300 K
α_{visc}		3.94, from optimization
$\alpha_{tension}$		1.96, from optimization

$\alpha_{\delta i}$		5.61, from optimization
$\alpha_{\delta e}$		0.543, from optimization
α_{mass}		1.05, from optimization
σ	Surface tension	$f(T_{wall})$, from IAPWS[35]
μ	Viscosity at the bubble wall	$f(T_{wall})$, from IAPWS[35]
ϕ_{flux}	Flux of vapor inside the bubble	$4\pi R^2 \frac{\alpha_{mass}}{\sqrt{2\pi M \tilde{R} T_{wall}}}(p_{sat} - p_B)$
T_B	Temperature inside the bubble	$f(E_B, \rho_B)$, from IAPWS[35]
k_B	Water conductivity in the bubble	$f(T_B, \rho_B)$, from IAPWS[35]
k_{wall}	Liquid water conductivity at the bubble wall	$f(T_{wall}, \rho_{wall})$, from IAPWS[35]
δ_i	Thickness of the inner heat transfer layer	$\sqrt{\frac{k_B R}{C_B \rho_B \sqrt{p_B/\rho_\infty}}}$
δ_e	Thickness of the outer heat transfer layer	$\sqrt{\frac{k_{wall} R}{C_{wall} \rho_{wall} \sqrt{p_{wall}/\rho_\infty}}}$
ΔH_{Lat}	Latent heat of vaporization at the bubble wall	$f(T_{wall})$, from IAPWS[35]
C_B	Heat capacity at constant pressure inside the bubble	$f(T_B, \rho_B)$, from IAPWS[35]
C_{wall}	Heat capacity at constant pressure at the bubble wall	$f(T_{wall}, \rho_\infty)$, from IAPWS[35]
p_{sat}	Saturation pressure at T_{wall}	$f(T_{wall})$, from IAPWS[35]
W_p	Work of pressure	$-p_{wall} 4\pi R^2 \dot{R}$
Q_{inter}	Heat flux at the bubble wall	$4\pi R^2 k_{wall} \frac{T_\infty - T_{wall}}{\alpha_{\delta e} \times \delta_e}$
Q_{mass}	Energy flux caused by mass transfer	$\dot{n} M \Delta H_{Lat}$
Q_{visc}	Viscous losses	$-4\alpha_{visc}\pi\mu R\dot{R}^2$
$Q_{tension}$	Work of surface tension	$-4\alpha_{tension}\pi\sigma R\dot{R}$

Q_{NP-w}	Heat transfer at the particle interface[42,48]	$4\pi R_{NP}^2 g \frac{\rho_B}{\rho_\infty}(T_{NP} - T_\infty)$
g	Heat transfer coefficient at the gold-water interface	$101.2\,10^6$ W/K/m^2, from the optimization
ρ_{NP}	Particle density (given for gold)	19,300 kg/m^3
C_{NP}	Particle heat capacity (given for gold[4])	$109.579 + 0.128T_{NP} - 3.4\,10^{-4}T_{NP}^2 + 5.24\,10^{-7}T_{NP}^3 - 3.93\,10^{-10}T_{NP}^4 + 1.17\,10^{-13}T_{NP}^5$ W/kg/K for T_{NP}<1337 K, constant above 1337 K
M	Molar mass of water	18g/mol
m_{molec}	Mass of one water molecule	$2.99\,10^{-26}$ kg
$\tilde{R}$	Gas constant	8.3145 J/mol/K

The equation system of Table S4 is solved with an implicit Backward Differentiation Formula solver with 10^{-4} relative and absolute tolerances. The initial conditions were determined in the previous section. The various coefficients involved in the equations are defined in Table S5.

As mentioned in main text, we do not use the enthalpy derived from the Tait equation of state[49], which assumes that the pressure is a function of the density only and independent of temperature. Since these thermal effects are important in our case, we used the enthalpy expression given by the IAPWS[35] equation of state. In consequence, instead of deriving the enthalpy like it is usually done in the context of the Gilmore equation, ($H = \int -\nabla\frac{p}{\rho}\mathrm{d}r = \int \frac{-\mathrm{d}p}{\rho}$, with $p(\rho)$ given by the Tait equation of state), we consider the IAPWS functional form for the density in function of the pressure and temperature: $\rho = f(p, T)$, and a pressure and temperature profile close to the bubble wall. The integration is then conducted numerically. The choice of the profile is not obvious, since little is known

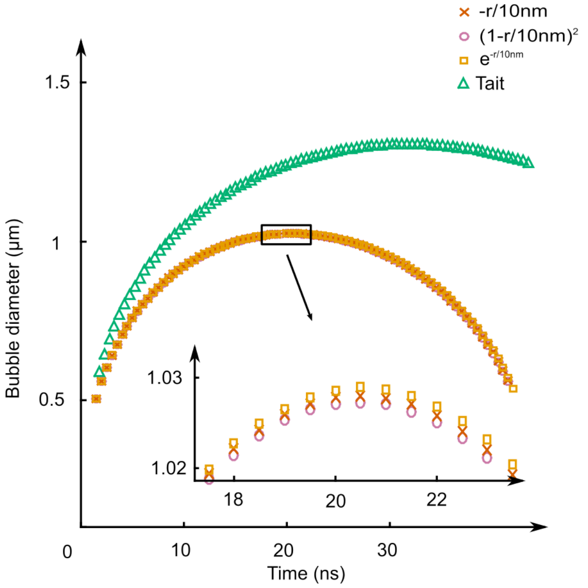

Figure S2 | Influence of the shape of the temperature profile chosen to calculate the enthalpy. Linear, exponential and quadratic profiles were tested and compared with the classical enthalpy given by Tait equation of state.

of the actual thermodynamic pathways followed by liquid water close to the wall. Here, we used a linear transition, similar to what was done in the bubble dynamics Sub-Model[46] $T(R(t)+r) = T_{wall} + \frac{T_\infty - T_{wall}}{\delta} r$. We chose $\delta = 10$ nm, in agreement with the values of δ_e given by our optimization. The sensitivity of the enthalpy to δ is in addition very weak, and this parameter is therefore not critical.

To investigate the sensitivity of the final bubble diameter on the temperature profile, we tested a quadratic ($T(R+r) = T_\infty + (T_{wall} - T_\infty)(1 - r/\delta)^2$) profile instead of a linear profile and observed how the diameter and dynamics of the bubble were impacted by this modification[41,50]. This did not significantly change final bubble diameter (Figure S2). Using an exponential profile (replacing the $(1 - r/\delta)^2$ by $\exp(-r/\delta)$) did not significantly impact the final result either. Using a linear profile seems thus reasonable. However, using the IAPWS equation of state instead of Tait's significantly modifies the bubble diameter, which demonstrates the importance of thermal effects on the bubble dynamics in our case.

IV Global optimization procedure

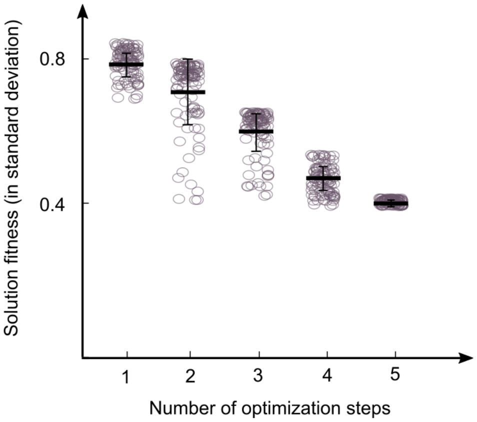

Figure S3 | Fitness of the top 100 solutions for successive optimization steps.

We used the NLopt implementation[51] of the COBYLA gradient-free optimizer[52] to optimize our 9 parameters, based on the minimization of the sum of squared residual relative to the experimental data. This procedure is performed in parallel from 40 randomly selected distinct starting points in the search space. Every 50,000 iterations, the search-space is reduced, based on the optimal parameters of the top 100 solution. For each step of 50,000 iterations, the top 100 solutions fitnesses are displayed on Figure S3. The best solution is around 0.4 times the experimental standard deviation and is shown in Figure 3a of the main text.

The resulting optimized values shown in Figure 2b,c of the article are very close to those found in the literature. For instance, the surface tension $\alpha_{tension}\sigma/R$ and the linear viscous term $\alpha_{visc}\mu\dot{R}/R$ are within 5% of the value commonly reported in the literature (2 and 4 respectively[53]). The optimal value for the layer heated by conduction h_T (0.72 nm) is also in very good agreement with previously reported results of 0.5 – 2 nm, obtained from molecular dynamics and hydrodynamic simulations[43,54]. Similarly, the coefficient of heat transfer at the gold-water interface, mass transfer at the bubble wall, g and α_{mass}, all lie relatively close to their reported values. In addition, the energy predicted to be transported in the shockwave agrees relatively well with experimental values acquired in slightly different conditions[45].

V Experimental fluence thresholds for cavitation

Experimental data presented in Figure 3c are given in Table S6.

Table S6 | Experimental fluences (with corresponding errorbars, in mJ/cm^2) for the cavitation threshold

	NP diameters (nm)						
Pulse widths	**81**	**109**	**123**	**151**	**175**	**195**	**213**
70 fs	191 (13)	137 (5)	119 (10)	77 (7)	79 (8)	80 (11)	107 (27)
500 fs	294 (15)	157 (11)	165 (12)	103 (13)	126 (10)	113 (19)	120 (29)
1 ps	342 (15)	174 (12)	182 (12)	126 (10)	141 (11)	134 (21)	142 (21)
2 ps	368 (18)	225 (21)	217 (37)	123 (15)	126 (10)	161 (17)	174 (24)
5 ps	294 (15)	256 (23)	241 (44)	182 (12)	157 (11)	282 (12)	210 (27)

VI Surface effects: behavior of small particles

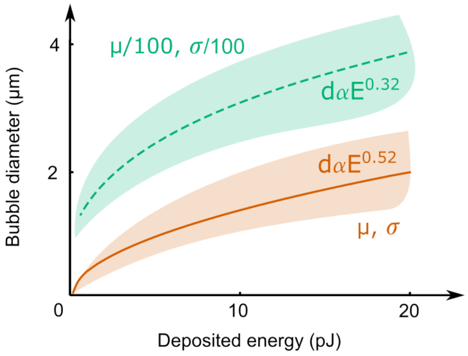

Figure S4 | Point cloud envelope and best fit for small bubbles for the normal model and for the model with viscosity and surface tension artificially reduced to a hundredth of their value.

As mentioned in the main text, we find a $d \, \alpha \, E^{1/3}$ dependency for bubbles bigger than 2 μm and a $d \, \alpha \, E^{1/2}$ one for smaller ones. In order to prove that the 1/2 coefficient is due to surface effects, we chose to artificially reduce the surface terms for surface tension and viscosity (Figure S4), by an arbitrary factor of 100. The $E^{1/3}$ dependency can be recovered when reducing the viscosity and the surface tension, which demonstrates that surface effects are at the origin of the $d\,\alpha\,E^{1/2}$ relation for smaller bubbles.

VII Scattering imaging technique, numerical simulation

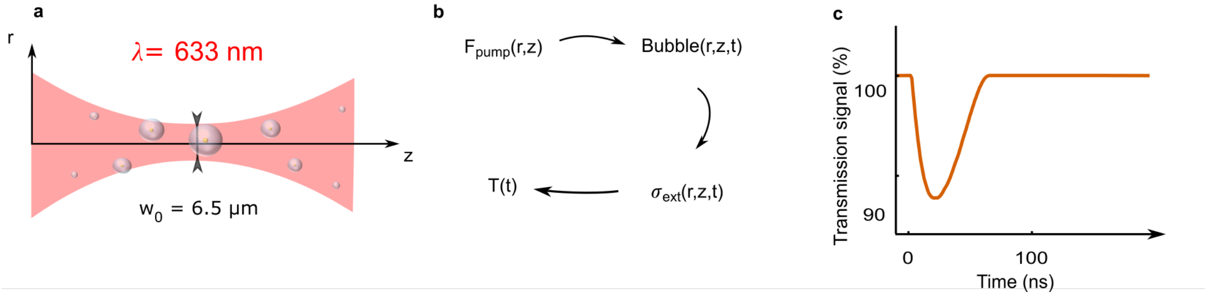

Figure S5 | Numerical reconstruction of the experimental probe scattering signal. **(a)** The Gaussian beam of the probe laser illuminates the solution. **(b)** The fluence of the pump laser is calculated at every point, leading to the calculation of the bubble dynamics and time-dependent extinction cross-section of the bubbles. Final integration yields the transient transmission signal, shown in **(c)**.

We simulated the experimental probe scattering signal using a parabolic beam propagation approximation and the experimental waist ($w_0 = 6.5\,\mu$m). Using a measured Rayleigh length of $z_R = 162\,\mu$m, and the expression for the Gaussian beam profile $w(z) = w_0\sqrt{1 + (\frac{z}{z_R})^2}$, the fluence can be deduced: $F(r,z) = 2F_0(\frac{w_0}{w(z)})^2 \exp(-\frac{2r^2}{w(z)}^{2})$, where F_0 is the average fluence. This z_R corresponds to the measured Rayleigh length of both pump and probe lasers. Given the particles geometry (78 nm SiO_2 core diameter – 28 nm Au shell) and the fluence, our multiscale framework calculates the bubble dynamics for every incident fluence. Assuming that the bubble is a spherical shell of refractive index 1 around the NP, we compute the extinction cross-section via Mie theory at each point (r,z) as a function of time (t). We assume that the probe laser intensity in water (I) follows a Beer-Lambert law, with a resulting transmission $I(t) = I_0 \exp(-A(t))$, where A accounts for the particle concentration and the time and space dependent extinction cross-section: $A(t) = \dfrac{1}{4\pi R^2}\displaystyle\int_{-L}^{L}\int_{0}^{R} c_0\,\sigma_{ext}\,(r,z,t)\,2\pi r\,\mathrm{d}r\,\mathrm{d}z.$ L and R are taken large enough so that a small variation does not affect the result (we used 300 μm and $1.5 \times w_0$). This methodology is summed up in Figure S5b and results in a curve like the one presented in Figure S5c. Note that the experimental asymmetry in the growth/collapse durations is recovered here. This asymmetry is due to the early participation and disappearance of the smaller, short-lived bubbles following the laser irradiation. A concentration of $2.7\,10^9$ NS/mL is taken, equal to the concentration used in experiments.

VIII Plasma temperature and density near the cavitation threshold

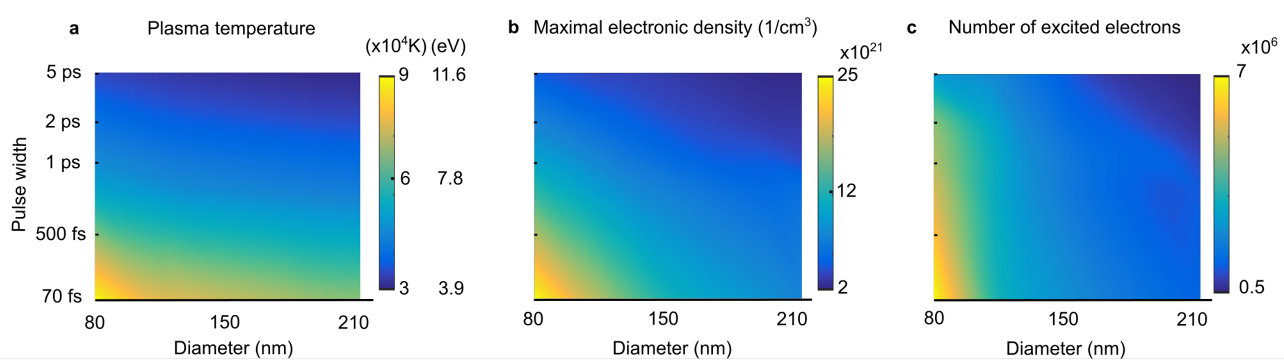

Figure S6 | Plasma composition for 1.04 μm bubbles. **(a)** Maximal plasma temperature. **(b)** Maximal electronic density. **(c)** Total number of excited electrons during the irradiation.

As illustrated in Figure S6a, the maximal temperature reached in the plasma at the cavitation threshold is nearly almost constant independent with of the pulse width, despite the large gap between energy deposition in the plasma for smaller and bigger particles. In particular, the value for fs pulses lies quite near the 5/4 times the gap value hypothesized derived by[10]. Furthermore, the commonly used cavitation criterion that identifies the cavitation onset with a plasma density of 10^{21} cm^{-3} seems inappropriate for cavitation around nanoparticles[10]. Indeed, Figure S6b shows that the maximal density can reach up to more than one order of magnitude above 10^{21} cm^{-3}, and that this density is not constant at all for all pulse widths and particle diameters. Figure S6c further examplifies the role of the plasma for smaller particles, with more than ten times more electrons excited for particles below 100 nm compared with particles above 150 nm.

References

1. Boulais, É., Lachaine, R., Meunier, M. Plasma mediated off-resonance plasmonic enhanced ultrafast laser-induced nanocavitation. *Nano Letters* **2012**, *12*, 4763–4769.

2. Stockman, M. I. Nanoplasmonics: past, present, and glimpse into future. *Optics Express* **2011**, *19*, 22029.

3. Chen, J. K., Tzou, D. Y., Beraun, J. E. A semiclassical two-temperature model for ultrafast laser heating. *International Journal of Heat and Mass Transfer* **2006**, *49*, 307–316.

4. Ekici, O. et al. Thermal analysis of gold nanorods heated with femtosecond laser pulses. *Journal of Physics D: Applied Physics* **2008**, *41*, 185501.

5. Qiu, T. Q., Tien, C. L. Heat transfer mechanisms during short-pulse laser heating of metals. *Journal of Heat Transfer* **1993**, *115*, 835.

6. Kittel, *Introduction to Solid State Physics*, Wiley, 2004.

7. Lin, Z., Zhigilei, L. V. Electron-phonon coupling and electron heat capacity of metals under conditions of strong electron-phonon nonequilibrium. *Physical Review B* **2008**, *77*, 1–17.

8. Ostrikov, K. K., Beg, F., Ng, A. Colloquium : Nanoplasmas generated by intense radiation. *Reviews of Modern Physics* **2016**, *88*, 011001.

9. Sacchi, C. A. Laser-induced electric breakdown in water. *Journal of the Optical Society of America B* **1991**, *8*, 337.

10. Vogel, A., Noack, J., Hüttman, G., Paltauf, G. Mechanisms of femtosecond laser nanosurgery of cells and tissues. *Applied Physics B* **2005**, *81*, 1015–1047.

11. Keldysh, L. V. Ionization in the field of a strong electromagnetic wave. *Journal of Experimental and Theoretical Physics* **1965**, *20*, 1307–1314.

12. Hallo, L., Bourgeade, A., Tikhonchuk, V. T., Mezel, C., Breil, J. Model and numerical simulations of the propagation and absorption of a short laser pulse in a transparent dielectric material: Blast-wave launch and cavity formation. *Physical Review B - Condensed Matter and Materials Physics* **2007**, *76*, 1–12.

13. Andreev, N. E., Veisman, M. E., Efremov, V. P., Fortov, V. E. The generation of a dense hot plasma by intense subpicosecond laser pulses. *High Temperature* **2003**, *41*, 594–608.

14. Veysman, M., Cros, B., Andreev, N. E., Maynard, G. Theory and simulation of short intense laser pulse propagation in capillary tubes with wall ablation. *Physics of Plasmas* **2006**, *13*, 1–11.

15. Link, S., Burda, C., Wang, Z. L., El-Sayed, M. A. Electron dynamics in gold and gold-silver alloy nanoparticles: The influence of a nonequilibrium electron distribution and the size dependence of the electron-phonon relaxation. *The Journal of Chemical Physics* **1999**, *111*, 1255.

16. Link, S., El-Sayed, M. A. Spectral properties and relaxation dynamics of surface plasmon electronic oscillations in gold and silver nanodots and nanorods. *The Journal of Physical Chemistry B* **1999**, *103*, 8410–8426.

17. Valle, G. D., Conforti, M., Longhi, S., Cerullo, G., Brida, D. Real-time optical mapping of the dynamics of nonthermal electrons in thin gold films. *Physical Review B* **2012**, *86*.

18. Stoll, T., Maioli, P., Crut, A., Del Fatti, N., Vallée, F. Advances in femto-nano-optics: ultrafast nonlinearity of metal nanoparticles. *The European Physical Journal B* **2014**, *87*, 260.

19. Werner, D., Furube, A., Okamoto, T., Hashimoto, S. Femtosecond laser-induced size reduction of aqueous gold nanoparticles: In situ and pump-probe spectroscopy investigations revealing coulomb explosion. *Journal of Physical Chemistry C* **2011**, *115*, 8503–8512.

20. Sun, C. K., Vallée, F., Acioli, L. H., Ippen, E. P., Fujimoto, J. G. Femtosecond-tunable measurement of electron thermalization in gold. *Physical Review B* **1994**, *50*, 15337–15348.

21. Carpene, E. Ultrafast laser irradiation of metals: Beyond the two-temperature model. *Physical Review B* **2006**, *74*, 024301.

22. Groeneveld, R. H. M., Sprik, R., Lagendijk, A. Femtosecond spectroscopy of electron-electron and electron-phonon energy relaxation in Ag and Au. *Physical Review B* **1995**, *51*, 11433–11445.

23. Del Fatti, N. et al. Nonequilibrium electron dynamics in noble metals. *Physical Review B* **2000**, *61*, 16956–16966.

24. Grua, P., Morreeuw, J., Bercegol, H., Jonusauskas, G., Vallée, F. Electron kinetics and emission for metal nanoparticles exposed to intense laser pulses. *Physical Review B* **2003**, *68*, 1–12.

25. Rosei, R. Temperature modulation of the optical transitions involving the fermi surface in Ag: Theory. *Physical Review B* **1974**, *10*, 474–483.

26. Lugovskoy, A. V., Bray, I. Ultrafast electron dynamics in metals under laser irradiation. *Physical Review B* **1999**, *60*, 3279.

27. Boutopoulos, C., Hatef, A., Fortin-Deschênes, M., Meunier, M. Dynamic imaging of a single gold nanoparticle in liquid irradiated by off-resonance femtosecond laser. *Nanoscale* **2015**, *7*, 11758–11765.

28. Johnson, P. B., Christry, R. W. Optical constants of the noble metals. *Physical Review B* **1972**, *6*, 4370–4379.

29. Docchio, F. Lifetimes of plasmas induced in liquids and ocular media by single Nd:YAG laser pulses of different duration. *Europhysics Letters (EPL)* **1988**, *6*, 407–412.

30. Lee, Y. T., More, R. M. An electron conductivity model for dense plasmas. *Physics of Fluids* **1984**, *27*, 1273.

31. Date, H., Sutherland, K. L., Hasegawa, H., Shimozuma, M. Ionization and excitation collision processes of electrons in liquid water. *Nuclear Instruments and Methods in Physics Research, Section B: Beam Interactions with Materials and Atoms* **2007**, *265*, 515–520.

32. Jackson, J. D. *Classical Electrodynamics, 3rd ed*, Wiley, 1999.

33. Mermin,, Ashcroft, *Solid State Physics*, Saunders, 1976.

34. Arnold, C. L., Heisterkamp, A., Ertmer, W., Lubatschowski, H. Computational model for nonlinear plasma formation in high NA micromachining of transparent materials and biological cells. *Optics Express* **2007**, *15*, 10303–10317.

35. IAPWS, *Thermodynamic properties of ordinary water substance for general and scientific use*, 2009.

36. Lyon, S. P., Johnson, J. D. *SESAME: The Los Alamos National Laboratory Equation-of-State Database*, 1979, pp ucrl–7118 and ucrl–52190.

37. Chowdhury, I., Xu, X. Heat transfer in femtosecond laser processing of metal. *Numerical Heat Transfer: Part A: Applications* **2003**, *44*, 219–232.

38. Smith, A. N., Norris, P. M. Influence of intraband transitions on the electron thermoreflectance response of metals. *Applied Physics Letters* **2001**, *78*, 1240–1242.

39. Guo, L., Hodson, S. L., Fisher, T. S., Xu, X. Heat transfer across metal-dielectric interfaces during ultrafast-laser heating. *Journal of Heat Transfer* **2012**, *134*, 042402.

40. Vogel, A., Busch, S., Parlitz, U. Shock wave emission and cavitation bubble generation by picosecond and nanosecond optical breakdown in water. *The Journal of the Acoustical Society of America* **1996**, *100*, 148.

41. Byun, K.-T., Kwak, H.-Y. A model of laser-induced cavitation. *Japanese Journal of Applied Physics* **2004**, *43*, 621–630.

42. Chapman, S. The Mathematical Theory of Non-Uniform Gases. 1962.

43. Sasikumar, K., Keblinski, P. Molecular dynamics investigation of nanoscale cavitation dynamics. *The Journal of Chemical Physics* **2014**, *141*, 234508.

44. Kotaidis, V., Dahmen, C., von Plessen, G., Springer, F., Plech, A. Excitation of nanoscale vapor bubbles at the surface of gold nanoparticles in water. *The Journal of Chemical Physics* **2006**, *124*, 184702.

45. Vogel, A. et al. Energy balance of optical breakdown in water at nanosecond to femtosecond time scales. *Applied Physics B* **1999**, *68*, 271–280.

46. Kreider, W., Crum, L. A., Bailey, M. R., Sapozhnikov, O. A. A reduced-order, single-bubble cavitation model with applications to therapeutic ultrasound. *The Journal of the Acoustical Society of America* **2011**, *130*, 3511–3530.

47. Lombard, J., Biben, T., Merabia, S. Ballistic heat transport in laser generated nanobubbles. *Nanoscale* **2016**, *8*, 14870–14876.

48. Siems, A., Weber, S. A. L., Boneberg, J., Plech, A. Thermodynamics of nanosecond nanobubble formation at laser-excited metal nanoparticles. *New Journal of Physics* **2011**, *13*, 22.

49. Gilmore, F. R. *The Growth or Collapse of a Spherical Bubble in a Viscous Compressible Liquid*, 1952.

50. Theofanous, T., Biasi, L., Isbin, H., Fauske, H. A theoretical study on bubble growth in constant and time-dependent pressure fields. *Chemical Engineering Science* **1969**, *24*, 885–897.

51. Johnson, S. G. The NLopt non-linear-optimization package. `http://ab-initio.mit.edu/nlopt`.

52. Powell, M. J. D. In *Advances in Optimization and Numerical Analysis*, Gomez, S., Hennart, J., Eds., Kluwer Academic: Dordrecht, 1994, pp 51–67.

53. Brennen, C. E. *Cavitation and Bubble Dynamics*, Oxford University Press, 1995.

54. Lombard, J., Biben, T., Merabia, S. Kinetics of nanobubble generation around overheated nanoparticles. *Physical Review Letters* **2014**, *112*, 105701.